Fatigue Crack Characteristics in Gradient Predeformed Pearlitic Steel under Multiaxial Loading

(article starts on next page)

Fatigue Crack Characteristics in Gradient Predeformed Pearlitic Steel under Multiaxial Loading

Daniel Gren,* Johan Ahlström, and Magnus Ekh

Rolling contact fatigue of railway rails not only severely deforms the surface material near the rail head, but also induces an anisotropy in the mechanical behavior due to work hardening and alignment of the microstructure along the shear direction. Cracks typically initiate in this region and propagate along the aligned microstructure. The fatigue behavior of rails is evaluated under uniaxial loading in the undeformed material state. However, this is not representative of the contact loading condition and material performance after years of service. Herein, the nonproportional multiaxial fatigue of as-received and biaxially predeformed pearlitic rail steel R260 is investigated. Four material states are investigated, corresponding to the microstructure found at different depths from the severely deformed surface material at the rail head. A starting notch is machined by electrical discharge machining to control crack initiation and allow for comparable surface crack propagation measurements. The crack path is found to be strongly influenced by the degree of predeformation while the early surface crack propagation rate is found to be similar for all material states.

1. Introduction

During operation, railway railheads are subjected to rolling contact fatigue loading. Large contact stresses occur at the rail/wheel interface as loads from passing trains are transmitted through the wheel to a small contact area on the rail head surface. The stresses generated by the wheel/rail contact are stochastic and complex to describe but can be characterized as being transient, multiaxial, and nonproportional. In the typical rolling contact fatigue loading, the stress state varies at each material point and the principal stress directions vary during one loading cycle.[1] Considering a simplified rolling contact loading condition, the normal stresses are compressive and pulsating with alternating out-of-phase shear stresses.[2] In addition, interfacial shear stresses induced by frictional forces from traction and cornering cause plastic deformation of both the rail head surface layer and the wheel tread. Frictional forces move the loci of maximum damage toward the surface.[1] When traffic conditions are predominantly unidirectional and frictional forces are high such that the stresses exceed the yield limit, shear strains accumulate, a phenomenon known as ratcheting.[3] This causes severe deformation of the material close to the rail head, significantly changing its properties and mechanical behavior due to work hardening and microstructure alignment, see, for example, refs. [4–7]. It is well known that the severely deformed surface material is the site of many damage categories such as squats and head checks.[8,9] The latter typically initiates once the ductility limit is reached and propagates under mixed mode loading along the direction of microstructure alignment. However, the effects of severe deformation on the material properties and the mechanical behavior of the surface layer are not well understood. Undeformed rail materials have been extensively tested under both uniaxial and multiaxial fatigue loading, see, for example, refs. [10–16]. Fatigue testing of undeformed rail material is important as delivered. However, it is not representative of the material performance of rail head surface layers after a period of service due to work hardening and microstructure alignment. In ref. [17], fatigue crack initiation of undeformed and predeformed R260 pearlitic rail steel was studied experimentally and crack initiation criteria were evaluated. But to the authors' knowledge, no multiaxial fatigue crack propagation studies of deformed rail material have been reported.

Pearlitic steels are widely used for railway rails due to their good combination of wear and strength relative to cost, and their properties can be tailored to fit operating conditions, see for example, refs. [18–23]. Within the range of rail grades used in Europe, the R260 steel is considered to be one of the softer grades. Compared to premium rail grades such as R350HT, which is head hardened, it results in more pronounced plastic deformation and wear.[24,25] To examine the material state of these steels after years of service, it is not possible to extract axisymmetric test bars with a well-defined microstructure from field

D. Gren, J. Ahlström
Division of Engineering Materials
Department of Industrial and Materials Science
Chalmers University of Technology
41296 Gothenburg, Sweden
E-mail: daniel.gren@chalmers.se

M. Ekh
Division of Material and Computational Mechanics
Department of Industrial and Materials Science
Chalmers University of Technology
41296 Gothenburg, Sweden

samples. This is because the severely deformed layer is shallow, has a strain gradient and is often cracked.

Previous studies have employed various techniques to replicate the highly deformed surface material on the rail head. The most common methods are high-pressure torsion (HPT), equal channel angular pressing (ECAP), and axial–torsion deformation. In these techniques, the material is deformed by applying a similar loading condition as that at the wheel/rail contact, that is, applying large shear deformation under high hydrostatic compressive stresses. The first reported replication of the severely deformed surface layer of R260 steel was done with ECAP by Wetcher et al.[26] Three deformed states were produced with equivalent shear strain ranging between 0.67 and 2. Subsequently, Hohenwarter et al.[27] Kammerhoffer et al.[28] and Leitner et al.[29,30] used HPT to deform the R260 rail steel to even higher equivalent strains. The main results of the studies showed that the fatigue crack propagation rate and fracture toughness under mode I loading strongly correlate with the direction of microstructure orientation, specifically the orientation of the ferrite–cementite lamellae relative to the crack plane. The main limitation with ECAP and HPT is that the extracted sample size must be small to have a well-defined and uniform microstructure. Thus, it is not possible to machine axi-symmetric test bars required for fatigue testing with ECAP and it is difficult to obtain by HPT. In order to enable fatigue testing, Meyer et al.[31] developed a method to reproduce the material state at the rail surface in which solid cylindrical test bars are twisted under a constant compressive load. This method can achieve shear strains up to 2.3, which is lower than what can be achieved with HPT, but has been shown to give a material structure representative of pearlitic rail steel at around 0.1 mm below the surface. By drilling the predeformed test bars to thin-walled tubular shape, the multiaxial elastoplastic as well as fatigue properties of deformed rail steels can be determined. In this study, a well-defined strain-controlled biaxial test series with out-of-phase loading was employed. The effect of predeformation on the crack propagation behavior under nonproportional multiaxial fatigue loading was investigated on massive cylindrical test bars.

2. Experimental Section

2.1. Material

In this article, multiaxial fatigue of the pearlitic rail steel R260 is studied. The R260 steel has an almost fully pearlitic microstructure and it has the nominal chemical composition listed in **Table 1**. The material was received as cylindrical rods with a diameter of 26 mm, extracted from new rails. Test bars, with the geometry and dimensions according to the drawing of **Figure 1**, were machined from these cylindrical rods.

Table 1. Nominal chemical composition of the R260 steel.

| C	Si	Mn	P	S	Cr	Al	V	N	Cu
0.72	0.31	1.04	0.006	0.010	0.02	<0.002	<0.005	0.006	0.018
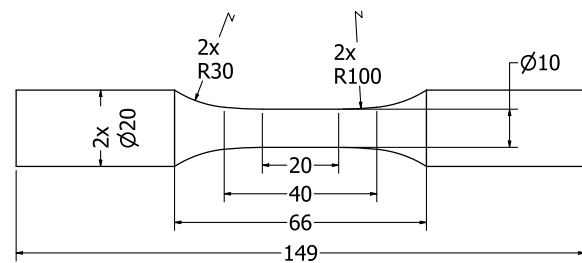
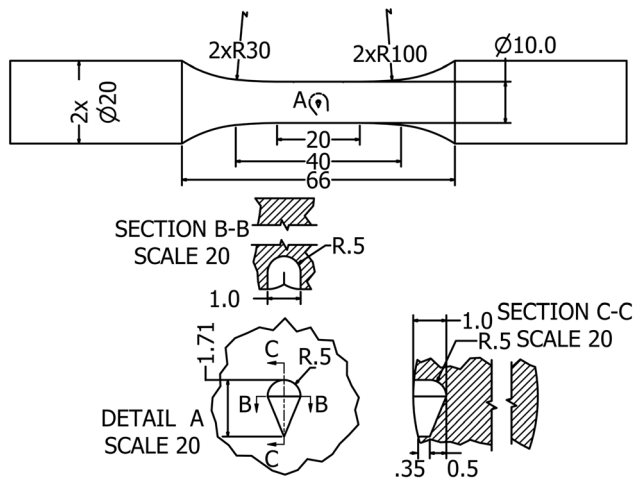**Figure 1.** Geometry and dimensions of test bars machined from cylindrical rods extracted from new rail heads.

2.2. Test Bars

The predeformation method developed by Meyer et al.[31] was employed in this study to replicate the material state in a region close to the surface of heavily deformed railheads. In the predeformation method, solid cylindrical test bars were repeatedly twisted in cycles of 90° under a constant compressive force, as described by the flowchart in **Figure 2**a. The compressive force was set to give an initial compressive stress of −500 MPa to prevent buckling and premature failure, noting that the compressive stress slightly decreased in each cycle as the diameter increased. In total, three deformed material states were produced, corresponding to twisting 1 × 90° (PD1), 3 × 90° (PD3), and 6 × 90° (PD6). The predeformed test bars' surface states corresponded to the material state found close to the railhead surface at different distances, with closer distance as the degree of predeformation increased. The exact distance cannot be stated as it depends on position on the rail head and how severely deformed the railhead is, but as a rough indication the PD6 surface shear strain corresponded to 0.1 mm depth below a heavily deformed rail surface and PD3 to 0.2 mm depth.[32] Test bars with the dimensions according to the drawing in Figure 1 were used for predeformation. These test bars were ground in steps to P1200 SiC abrasive paper to avoid premature failure during predeformation. In addition, undeformed test bars denoted PD0 were included in this study as a reference.

Test bars subjected to the predeformation method underwent geometry changes, where the length/width ratio decreased, making these test bars unsuitable for fatigue testing. Thus, to enable fatigue testing, all predeformed test bars were reprofiled according to the drawing in Figure 1. Two sets of test bars were prepared, notched, and smooth. The notch was machined by electrical discharge machining (EDM) at the center of the gauge section, following the dimensions specified by the drawing in **Figure 3**. The notch geometry was designed to promote crack initiation in the same material volume for both axial and torsional loading. With crack initiation from one side, it is possible to choose a smaller field of view of the camera which enables better resolution of the initiating surface crack. In addition, two small indents for the extensometer with a spacing of 12 mm across the center of the gauge section were machined for both sets of test bars. The indents were made to ensure good surface contact of the extensometer pins. In the case of the notched samples, the indents were machined 90° from the notch center, toward the rounded side of the notch to allow crack monitoring. Prior to making the notch and indents, all test bars were mirror polished
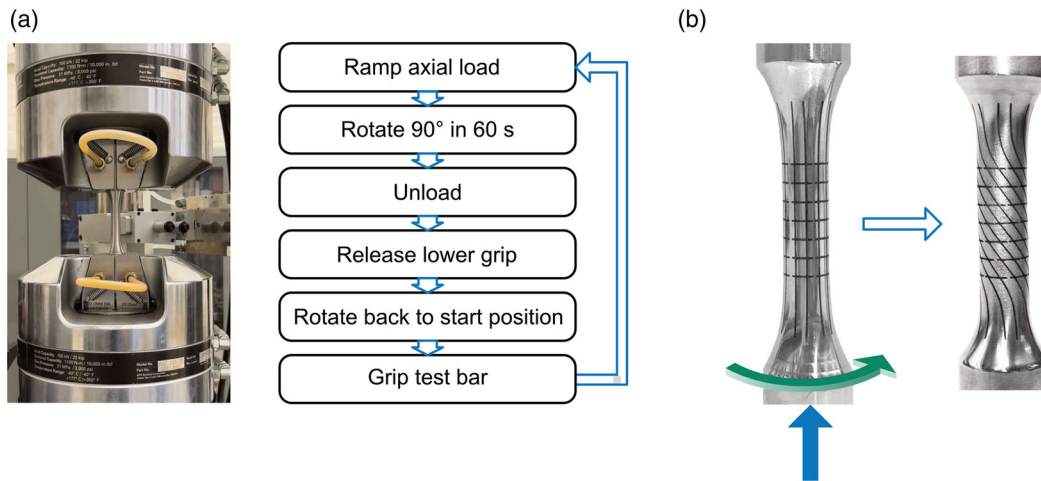
Figure 2. Predeformation method: a) flowchart describing the predeformation process and b) visualization of shear deformation resulting from twisting the test bar $3 \times 90°$ (PD3).

Figure 3. Geometry and dimensions for notched test bars used in the fatigue crack propagation experiments.

In a previous study by the author,[33] the surface shear strain of PD3 and PD6 test bars after predeformation was measured to be 0.74 ± 0.05 and 1.52 ± 0.5 respectively. The diameter after predeformation was 10.64 and 11.06 mm for PD3 and PD6, respectively. The shear strain γ was computed from (see[33]) Equation (1)

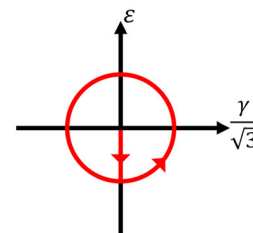$$\gamma = \left(\frac{\tan(90° - \alpha)}{R} \right) r \tag{1}$$

where α is the angle between the flow lines and the axial direction, R is the radius after predeformation, and r is the radius after reprofiling. Hence, the surface shear strain for the PD3 and PD6 test bars used in this study can be estimated to be 0.7 ± 0.05 and 1.38 ± 0.05 respectively. Assuming similar shear strain levels after each predeformation cycle, the surface shear strain of the PD1 test bars can be estimated to be 0.23.

2.3. Design of Experiments

In this study, the effect of predeformation on crack propagation behavior under rolling–contact-like loading conditions was studied. For this purpose, the crack propagation experiments were conducted under nonproportional multiaxial fatigue loading with a phase difference of 90°. The fatigue experiments were strain controlled and conducted with a nominal equivalent von Mises strain amplitude of 0.6%, calculated according to Equation (2)

$$\varepsilon_{eq} = \sqrt{\varepsilon^2 + \frac{\gamma^2}{3}} \tag{2}$$

Axial and torsional strain was set to 0.424% and 0.735%, respectively, to give a circular strain path in the ε versus $\gamma/\sqrt{3}$ strain space, as shown in **Figure 4**. The waveform for the axial and torsional loading was sinusoidal and the frequency was set to 0.2 Hz to avoid adiabatic heating due to the large plastic strain amplitude. The fatigue experiments continued until the fracture or instability in the control system due to the large decrease in stiffness for large cracks. The servohydraulic axial-torsion system MTS 809, with an axial and torsional load capacity of ± 100 kN and ± 1100 Nm load cell, and displacement and rotation ranges of ± 75 mm and $\pm 90°$, was used for the predeformation and fatigue experiments. The extensometer for controlling the strain was MTS 632.68F-12.

Figure 4. Strain path for nonproportional loading (90° phase difference).

**ADVANCED
SCIENCE NEWS**

www.advancedsciencenews.com

**ADVANCED
ENGINEERING
MATERIALS**

www.aem-journal.com

Table 2. Test matrix.

| Material state	Loading path	ε_{eq} [%]	No. of notched test bars	No. of smooth test bars
PD0	Non-proportional loading 90°	0.6	2	1
PD1	Non-proportional loading 90°	0.6	2	1
PD3	Non-proportional loading 90°	0.6	2	1
PD6	Non-proportional loading 90°	0.6	2	1

The test plan for the fatigue and fatigue crack propagation experiments is given in **Table 2**. Two test bars of each material state were used in the fatigue crack propagation experiments while one test bar of each material state was used in the fatigue experiments.

2.4. Hardness Measurement

The hardness distribution after fatigue testing of the smooth test bars was measured with the hardness tester Durascan 40 G5 from Struers/Emcotest using the Vickers method. The smooth test bars were sectioned across the center of the gauge section and two specimens, one from each side of the cut were sectioned out. In total, hardness was measured on eight samples, two for each material state on the cross section facing the center of the gauge section. **Figure 5** shows the indentation pattern used for measuring the hardness distribution on the axial cross section on a polished surface. The applied load was 5 kgf (HV5) with a dwell time of 15 s and the indent was measured using a $50\times$ objective lens.

2.5. Digital Image Correlation

In this study, digital image correlation (DIC) measurements were conducted using the VIC-3D stereo microscope (Olympus
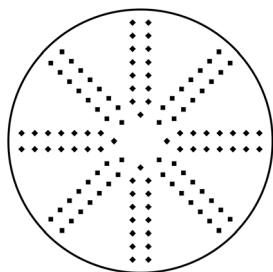
Figure 5. Indent pattern used for characterizing the hardness gradient after nonproportional fatigue loading.
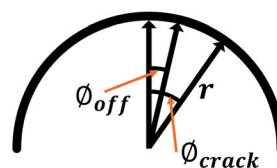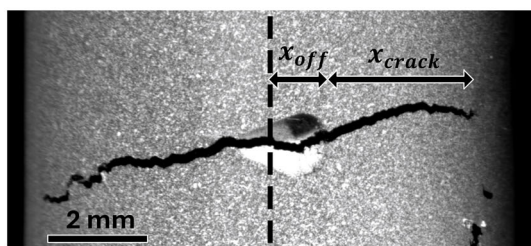
Figure 6. Illustration of crack measurement.

SZX16) system provided by Correlated Solutions to analyze the strain field during crack propagation in two notched test bars, PD0 and PD6. This technique is based on correlating deformed images with a reference image and requires a random speckle pattern to be applied to the surface to be measured. The speckle pattern was applied with an airbrush in two steps, first a white layer was applied and after drying fine speckles of black paint were sprayed onto the surface. The magnification was set to 0.96x, corresponding to a field of view of 7.29×8.85 mm. The reference image was acquired at zero load after gripping the test bar in the axial-torsion machine. After the DIC measurements, the strain field was determined and analyzed using the VIC-3D software.

2.5.1. Crack Propagation Measurement

During the fatigue crack propagation experiments, the surface crack length was measured using the 3D DIC stereo microscope system provided by Correlated Solutions. Images and load signals (axial and torsional channels) were acquired simultaneously at a frequency of 2 Hz, corresponding to 10 images per load cycle. The acquisition rate was sufficient to resolve the sinusoidal load wave, so that for each load cycle the crack was acquired close to the peak axial load. A MATLAB script was written to sort out the images close to the peak axial load for each cycle, where the crack was almost fully open, facilitating crack propagation measurement. The magnification used during image acquisition was adjusted according to the crack length within the range 0.6–1.2x, starting with highest magnification during early crack growth. The crack was measured on both sides of the notch every 16th cycle after detection, as shown in **Figure 6**. The crack length is defined as the distance from the edge of the notch to the circumferential position of the crack tip along the surface, irrespective of any inclination in the axial direction. As the surface was curved, it was necessary to correct the crack length for the curvature of the surface. This was done by first measuring x_{off} and x_{crack} relative to the center line and then calculating ϕ_{off} and ϕ_{crack} according to Equation (3)

$$\phi_{off/crack} = \arcsin\left(\frac{x_{off/crack}}{r}\right) \qquad (3)$$

Thereafter, the true crack length, defined as the crack length on the mantle surface, in the horizontal direction, can be determined by equation (4)

$$\text{Crack length}_{true} = (\phi_{crack} - \phi_{off}) \cdot r \qquad (4)$$

3. Results

3.1. Mechanical Response

The evolution of the nominal axial stress amplitude and mean stress for the notched and smooth test bars is shown in **Figure 7**. When interpreting the results for the smooth specimens, it should be noted that the number of cycles to failure is somewhat underestimated as these test bars fractured at the extensometer indents which constitute stress raisers.

Comparing the notched and smooth test bars of the same material state reveals minimal differences in both axial stress amplitude and mean stress for the first 500 cycles. However, beyond this point, the propagating crack in the notched specimens is long enough to affect the load carrying capacity, resulting in a drop in axial stress amplitude. The surface crack length at 500 cycles is ≈2 mm on each side of the notch, as shown in Figure 14. The similar axial stress amplitude for the notched and smooth specimens indicates that the highly multiaxially (out-of-phase) strained region in front of the crack strain hardens and compensates for the reduced load area. The differences observed between the undeformed and predeformed material are the load ratio and magnitude of the axial stress amplitude. The undeformed material shows lower stress amplitudes compared to the predeformed material, where the amplitude increases with the degree of predeformation. The load ratio
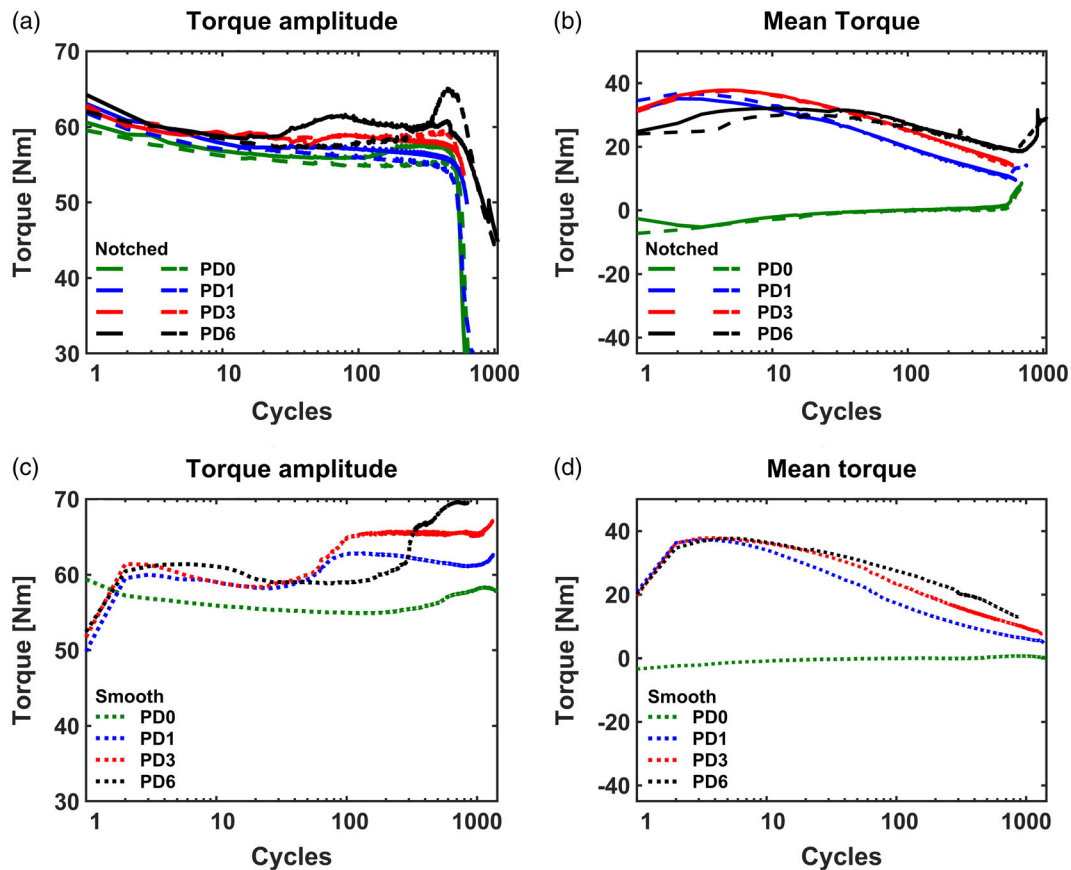
for the undeformed material is close to −1, resulting in an almost fully reversed axial load. In contrast, the predeformed material experiences an asymmetric load, with peak compressive stress larger than peak tensile stress.

The evolution of the torque response for the notched and smooth test bars is shown in **Figure 8**. As the test bars are cylindrical, the magnitude of the shear stress, that varies along the radius, cannot be determined without material modeling assumptions and finite-element analysis, see, for example ref. [17]. The torque response is not as straightforward to analyze as the axial stress response, particularly for the notched specimens. As the crack propagates, the torque response is also influenced by the crack face friction, which is influenced by crack topography and wear of the crack faces.

By comparing the torque response for the notched and smooth test bars of the same material state, a difference in the torque amplitude is observed. The torque amplitude of the notched predeformed test bars slightly decreases during the first 500 cycles followed by a rapid decrease as the crack propagates, with an exception for one PD6 test which shows an increase in torque amplitude. The torque amplitude response for the predeformed test bars is thought to be a consequence of the fact that the crack propagation reduces the structural integrity more than the strain hardening in front of the crack can compensate for, as explained in the result for the axial stress response. In contrast, the torque amplitude for the smooth predeformed test bar initially increases,
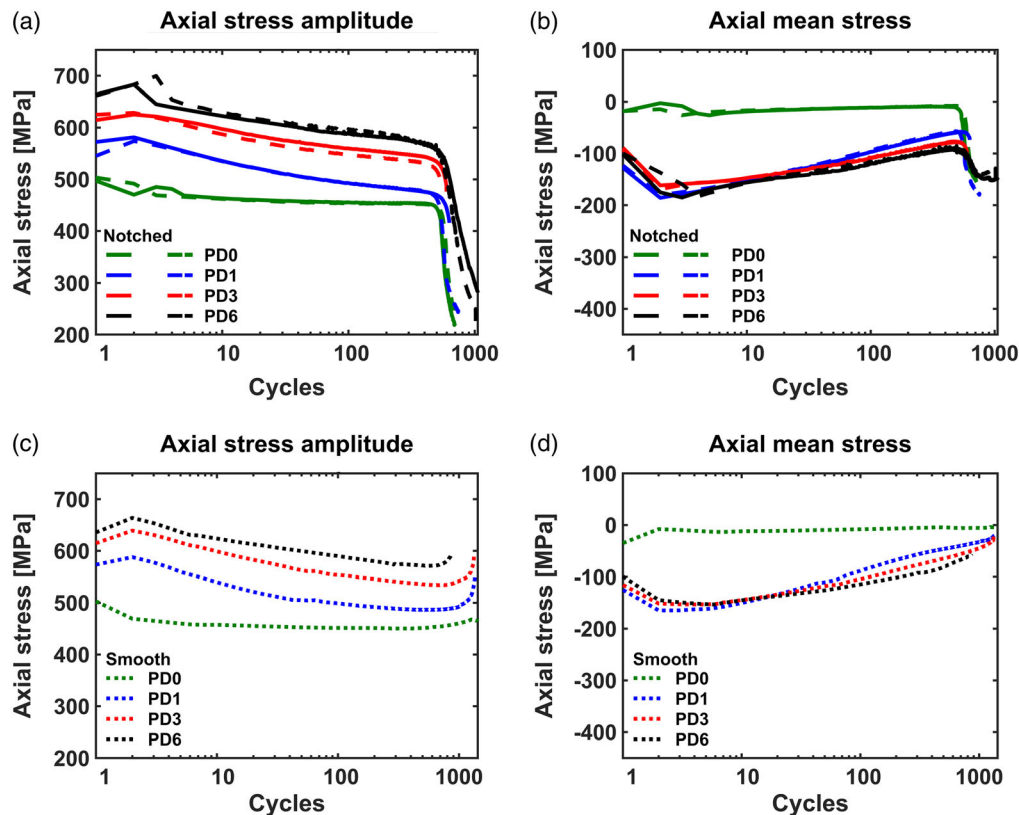
Figure 7. Comparison between the axial stress evolution of notched and smooth test bars at $\varepsilon_{eq} = 0.6\%$: a) and b) the axial stress amplitude and the axial mean stress with respect to the number of cycles for notched test bars. c) and d) the axial stress amplitude and the axial mean stress with respect to the number of cycles for smooth test bars.

ADVANCED
SCIENCE NEWS

www.advancedsciencenews.com

ADVANCED
ENGINEERING
MATERIALS

www.aem-journal.com

Figure 8. Comparison between the torque evolution of notched and smooth test bars for nonproportional loading at $\varepsilon_{eq} = 0.6\%$: a) and b) the torque amplitude and the mean torque with respect to the number of cycles for notched test bars. c) and d) the torque amplitude and the mean torque with respect to the number of cycles for smooth test bars.

followed by saturation and subsequent hardening and saturation. The undeformed smooth material instead initially decreases followed by a continuous increase for the remaining cycles.
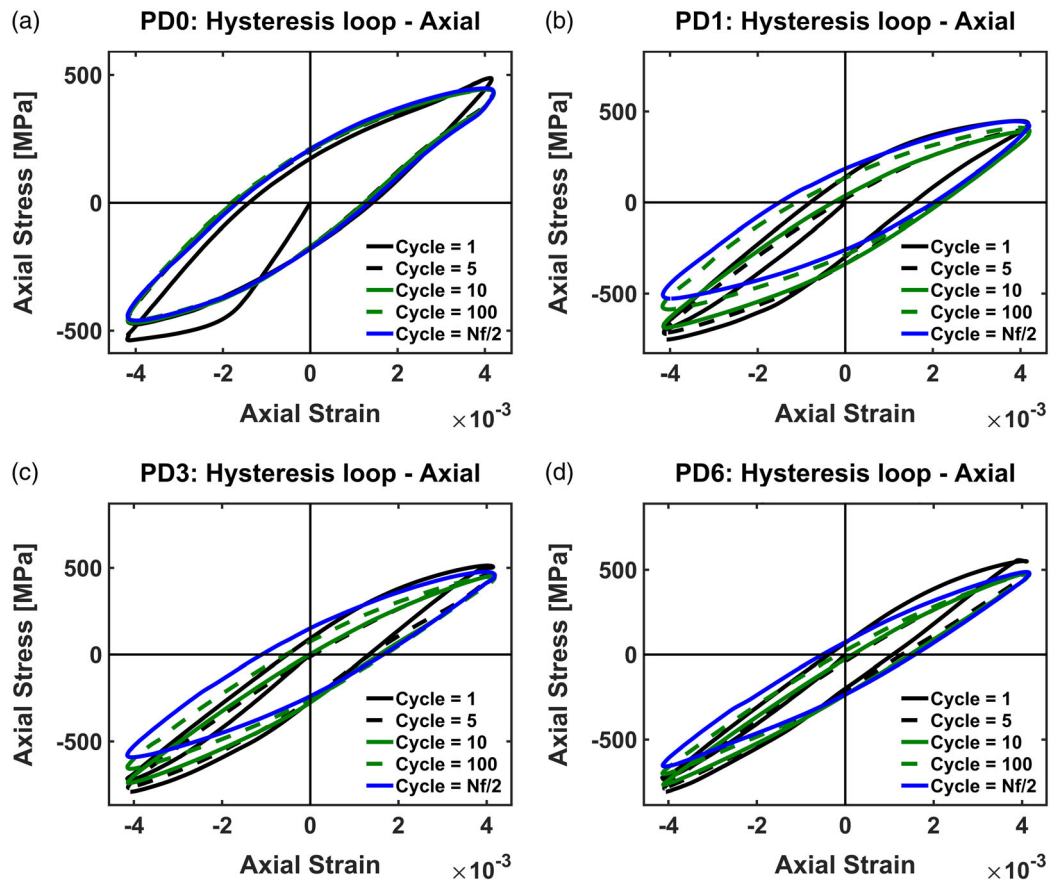
The mean torque response is similar for both smooth and notched test bars when comparing the same material state. The mean torque initially increases for the predeformed material followed by a decrease where the smooth test bars almost reach zero mean torque. In contrast, the mean torque for the undeformed material remains close to zero throughout the test. Combining the torque amplitude with the mean torque, it can be observed that the undeformed material exhibits an almost symmetric torque response whilst the predeformed material experiences an asymmetric torsional response toward positive torque, similar to what was observed for the axial stress response.

Figure 9 and **10** show the hysteresis loops for axial stress and torque, respectively, for the smooth specimens. The axial plastic strain amplitude estimated as the hysteresis loop width is observed to be almost constant for all material states while the torsional plastic strain amplitude increases after the initial 10 cycles for the predeformed material but remains almost constant for the undeformed material. The main difference in the axial stress response is seen during compression, where the compressive stress for the predeformed material is initially significantly higher than for the undeformed material. The tensile stress

response seems not to vary much with predeformation. The main difference in the torque response between the undeformed and predeformed material is seen at positive torque loads. The torque response is similar for the different predeformed material states, as shown in Figure 8.

3.2. Hardness Measurement

The hardness distribution along the radial direction for the smooth test bars is shown in **Figure 11**. The predeformed material states show a hardness gradient. The hardness gradient results from the predeformation where the degree of deformation varies along the radial direction as an effect of the shear strain distribution which varies linearly along the radial direction, decreasing toward the center. In a previous study, the authors[33] measured the hardness gradient for PD3 and PD6 after predeformation. Comparing the results with this article, the hardness gradient of the predeformed material is ≈10 HV5 units lower after fatigue testing. The hardness gradient of PD1 after predeformation has not been measured, but based on the axial stress and torque amplitude following the same trend as PD3 and PD6, it is expected to be slightly lower after fatigue than after predeformation.

ADVANCED
SCIENCE NEWS
www.advancedsciencenews.com

ADVANCED
ENGINEERING
MATERIALS
www.aem-journal.com

Figure 9. Hysteresis loop, showing the axial stress–strain response for smooth test bars of different material states under nonproportional loading conditions, with an equivalent strain of $\varepsilon_{eq} = 0.6\%$: a) PD0, b) PD1, c) PD3, and d) PD6.

During monotonic pre straining, shear deformation causes increase in hardness in proportion to the radial distance from the center, due to work hardening and decreased interlamellar spacing.[34] During subsequent fatigue loading in the plastic range, the axial stress amplitude decreases after the initial increase at cycle 2. The multiaxial straining is valid only in a rather thin surface layer; at larger depth the shear strain is not large enough to cause plastic deformation hardening. The force response is an integration of axial stresses over the cross section, and the supposedly higher stresses in the very surface layer are hidden in the average.
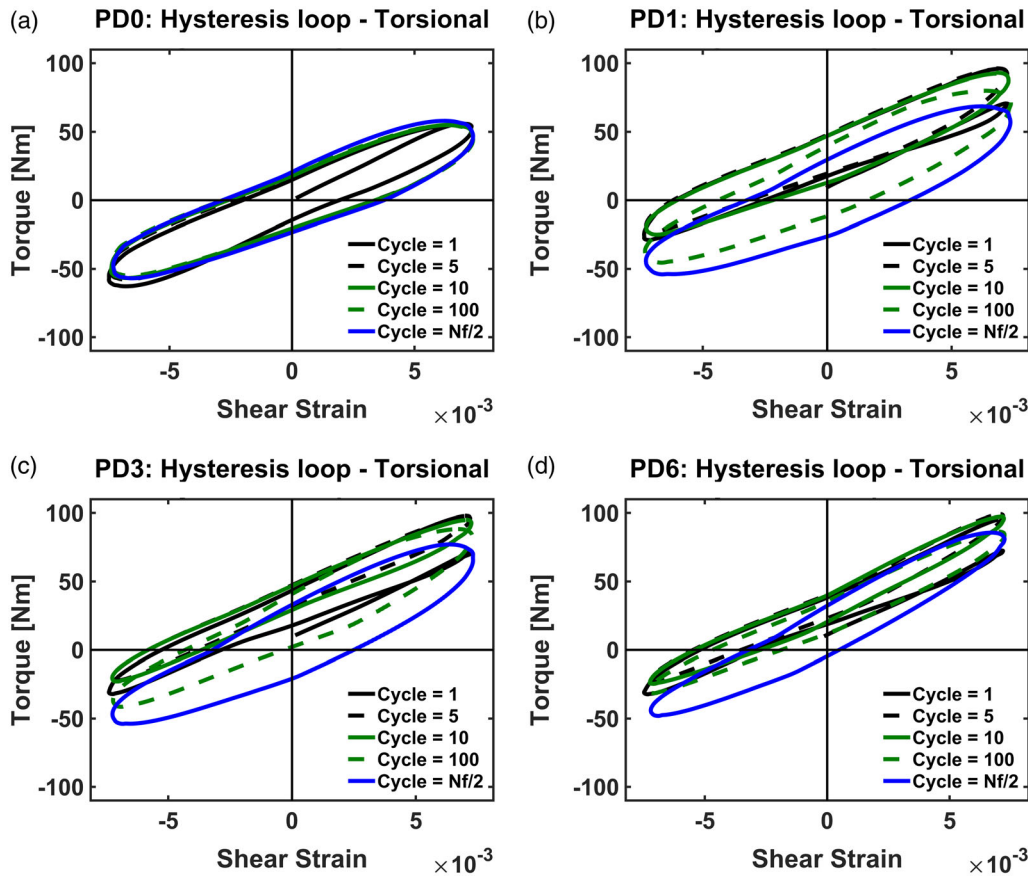
The multiaxial fatigue behaviors of the predeformed states have not been previously investigated but characterized for the rail steel R350HT under uniaxial, in-phase, and out-of-phase multiaxial loading by Dhar et al.[14] The dislocation density was the highest after out-of-phase loading and the dislocation structure was tangled. Initial hardening followed by softening and saturation was observed for this loading condition. In the light of these findings, it is thought that the softening behavior observed in Figure 7 and 11 may be attributed to either or a combination of dislocation ordering and annihilation of dislocations by dynamic recovery. However, to explain the softening mechanism, the dislocation structure and density must be investigated.

3.3. Crack Propagation Measurements

In **Figure 12** and **13**, the surface crack length measurements are plotted against the number of measurements since a visible crack first appeared, to make the crack propagation rate comparable. In **Figure 14**, the crack length measurements with respect to the number of cycles are shown. The figures show the surface crack length measured from the left and right side of the notch. The crack was always observed to initiate first at the left side of the notch, as intended, see Figure 3. Crack initiation on the left side was followed by subsequent propagation away from and into the notch. A crack on the right side initiated after the left crack propagated some distance. Similarly, a crack that initiated on the right side propagated away from and into the notch. The cracks on the left and right side merged into a single crack after reaching several millimeters length, as measured on the surface.

The crack propagation rates for the undeformed and predeformed material are very similar, as shown in Figure 12 and 13. However, due to the variation between each duplicate test, it is difficult to determine if there is a significant difference in the crack propagation rate. A noticeable difference between undeformed material and PD6 can only be observed when the crack is longer, $\approx 2\,mm$ on each side. The results also indicate

2400950 (7 of 13)

ADVANCED
SCIENCE NEWS

www.advancedsciencenews.com

ADVANCED
ENGINEERING
MATERIALS

www.aem-journal.com

Figure 10. Hysteresis loop, showing the torque–strain response for smooth test bars of different material states under nonproportional loading conditions, with an equivalent strain of $\varepsilon_{eq} = 0.6\%$: a) PD0, b) PD1, c) PD3 and d) PD6.
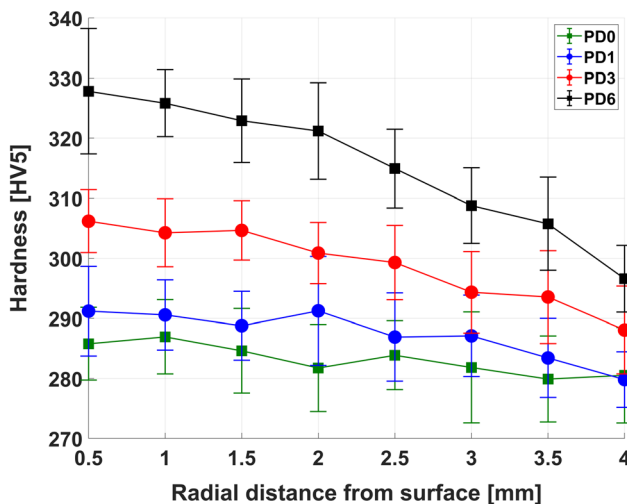

Figure 11. Hardness distribution as a function of radial distance after nonproportional fatigue loading of smooth test bars of different material states.

that the crack propagates at a higher rate in the undeformed material compared to PD1 and PD3, although the difference is not as significant as the difference between PD0 and PD6. Another difference observed is that the crack initiates earlier

in the predeformed material than in the undeformed material, as shown in **Figure 14** and **15**.

The inset of Figure 12 shows the early crack growth from the sharp left side of the notch. In the early stages of crack growth, the crack grows close to the mantle surface where the shear deformation for the predeformed material is at its highest. Interestingly, the rate of crack propagation is very similar. From the fatigue crack propagation measurements conducted on severely deformed pearlitic rail steel R260 by Leitner et al. in refs. [29,30], the crack propagation resistance was found to be dependent on the orientation of the crack plane relative to the microstructure alignment. The highest resistance to crack propagation was found when the crack propagated transverse to the microstructure alignment. The early crack growth on the left side for the predeformed material states is almost horizontal and the crack thus grows at an angle to the direction of microstructure alignment. Nevertheless, the crack propagation rate was found to be similar to that of PD0. The torque and axial load response is higher for the predeformed material and thus the effective load at the crack tip will be different which could partly explain why a similar crack propagation rate is observed. However, as the crack depth, that is, the location of the crack front, could not be measured, the surface crack length measurements should not be viewed as a representative measure of the overall crack growth. At the surface, the stress state is plane
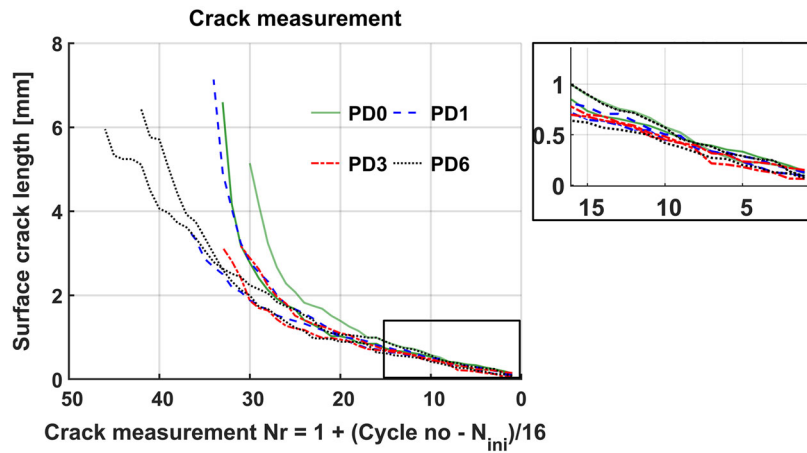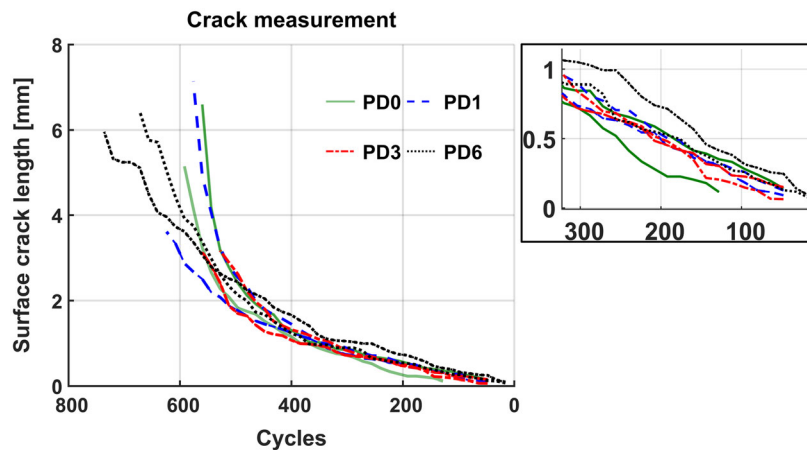
Figure 12. Figure showing the left crack length with respect to the crack measurement number. The inset shows the early surface crack propagation. The first crack measurement was made once the crack could be detected.
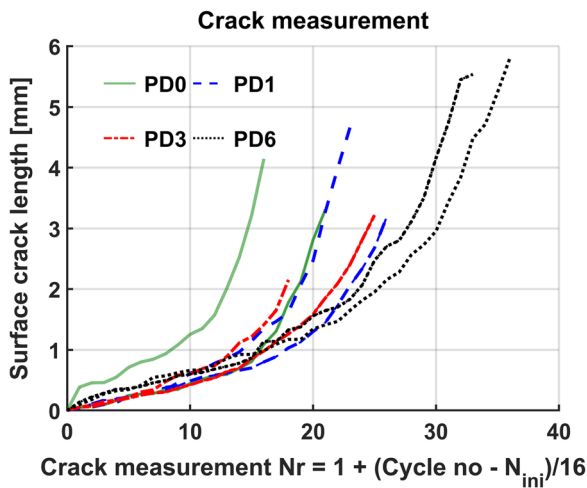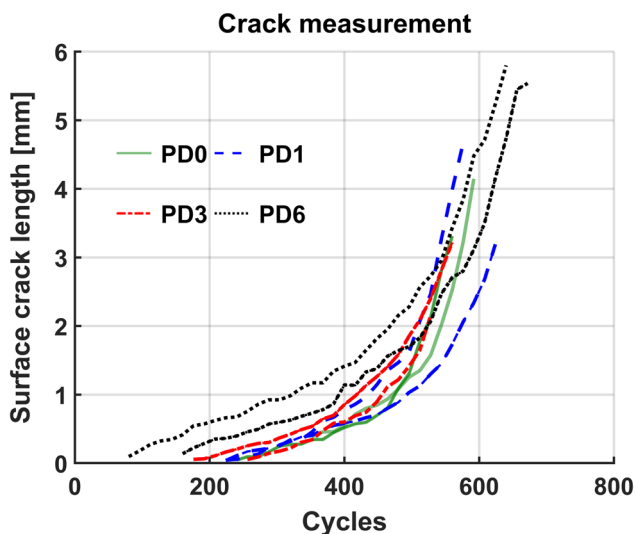

Figure 13. Figure showing the left crack length with respect to the crack measurement number. The first crack measurement was made once a crack could be detected.

stress, whereas in the bulk, the stress state becomes more plane-strain like. It may therefore be expected that the surface crack growth rate will be different from that within the bulk. Nevertheless, it is expected that the comparison of early crack growth will be comparable as the crack propagates horizontally and mainly near the circumference.

The yield surface of the predeformed material state was experimentally determined by Meyer et al.[35] It was found that predeformation causes the yield surface to expand and shift with respect to the undeformed material state. Consequently, the out-of-phase multiaxial loading results in varying degrees of plastic deformation for the predeformed material state, which affects the amount of damage induced in each loading cycle. In the initial stages of crack growth, the crack was observed to be almost horizontal for all material states, as illustrated in **Figure 16**. Given that the cracks are relatively short in comparison to the notch, the local stress field at the crack front is affected by the notch. Furthermore, a residual stress state is anticipated in the vicinity of the notch due to machining and predeformation. However, the nature of the stress state is unknown, but

Figure 14. Figure showing the left crack length with respect to load cycle number. The inset shows the early surface crack propagation.

**ADVANCED
SCIENCE NEWS**

www.advancedsciencenews.com

**ADVANCED
ENGINEERING
MATERIALS**

www.aem-journal.com

Figure 15. Figure showing the right crack length with respect to load cycle number.

it is expected to partly relax upon plastic deformation. Consequently, the early stages of crack propagation are not solely influenced by the material state and loading condition. This could explain why a similar crack propagation rate was observed.

As the crack propagates, the effect of the notch decreases and when the crack is continuous from one side to the other, the effect of crack growth is limited even if crack closure could be affected. It was observed in the experiments that the crack path is highly dependent on the material state, as shown in Figure 16. The crack growth patterns for PD3 and PD6 are significantly

different from those observed for PD0 and PD1. Therefore, the stress intensity at the crack tip will be different due to the orientation of the crack front in relation to the applied load. Furthermore, the stress intensity will vary depending on the applied load, which differs between the material states due to strain-controlled loading. Consequently, the local stress state will be different, which will affect the rate of crack propagation.

The crack propagation rate of the pearlitic rail steel R260, severely deformed by HPT and equal-angular channel pressing, was investigated by Leitner et al.[30] and Wetscher et al.[26] The crack propagation rate was found to be strongly correlated to the orientation of the crack plane relative the microstructure alignment. The microstructure of the predeformed material states in this study aligns toward the shear plane; however, the degree of predeformation is insufficient to fully align the microstructure in the bands of cementite lamellae of similar orientation. Based on the experiments conducted by Leitner et al.[30] and Wetscher et al.[26] the crack propagation rate would be higher in PD6 as compared to PD3 as the crack propagates along a weaker path; see structural alignment with respect to the crack path in Figure 16c,d. However, as the crack path is significantly different between PD0, PD3, and PD6, it is not possible to make a direct comparison of the crack propagation rate as the stress intensities are different.

3.4. Crack Path

The crack paths for the different material states are shown in Figure 16. It is evident that predeformation has a significant effect on the crack path, suggesting that predeformation may govern the crack growth behavior. An increasing predeformation shifts the crack plane from the case with isotropic material PD0
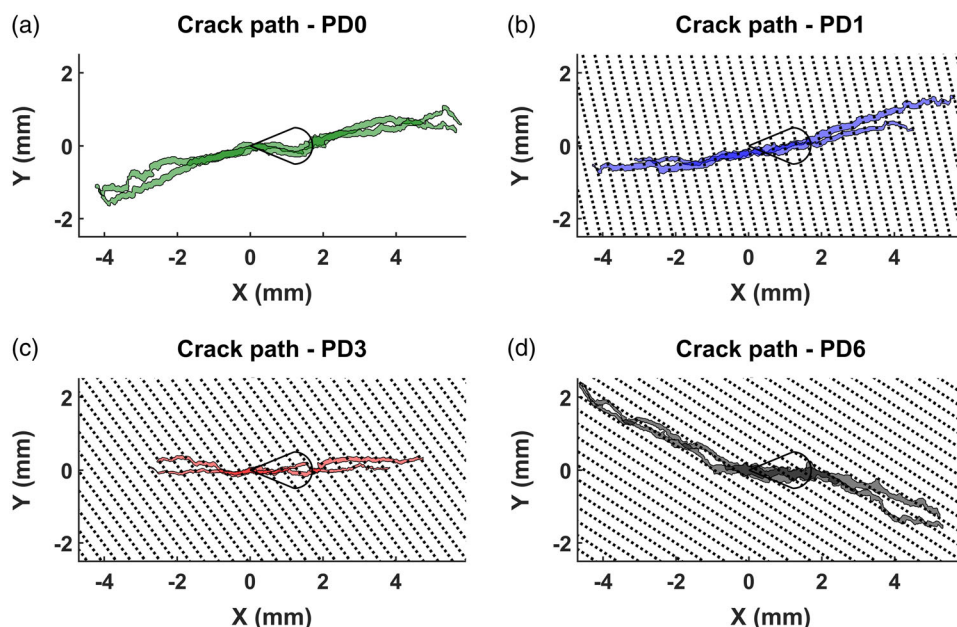
Figure 16. Crack path for a) PD0, b) PD1, c) PD3, and d) PD6. The crack path is a 2D projection of the surface crack. The origin is set at the left side of the notch as the crack first initiates there. Note that $\times$ is the projected distance from the origin. The overlayed grid in (b–d) represents the magnitude of surface shear deformation resulting from predeformation.

ADVANCED
SCIENCE NEWS

www.advancedsciencenews.com

ADVANCED
ENGINEERING
MATERIALS

www.aem-journal.com

toward an orientation more parallel to the shear planes, for example, PD6. Consequently, the resulting crack path is thought to be governed by the predeformation level. The difference between the undeformed material PD0 and PD1 is small. Both show an inclined crack growth, but the crack propagates at a slightly shallower angle for PD1. However, as the degree of predeformation increases to PD3, a marked difference is observed. The crack propagates transversely to the direction of the microstructure alignment resulting from the predeformation. In addition, the final crack length prior to fracture is much shorter as compared to the other material states.

In the case of the material state PD6, the crack path is almost the mirror image of that of PD0, but with an even steeper inclination angle, clearly showing an effect of predeformation with the crack growing more toward the direction of microstructure alignment. Since the microstructure is random and the mechanical properties can be assumed to be isotropic for PD0, the crack inclination only results from the loading case. In the Appendix, Figure A1, and A2 highlight the difference in surface crack path

between PD0 and PD6 where the surface crack growth in the latter shows a spiral crack path. Based on the spiral crack path, the continuous crack front cannot be semielliptical as observed for material states PD1 and PD3, as shown in Figure A3 in appendix. However, as the final fracture of the PD6 test bar did not propagate along the continuous crack front, we were unable to separate the crack surfaces to examine the fatigue zone. However, based on the fracture toughness and fatigue crack propagation measurements predeformed on severely deformed pearlitic rail steel R260 by Wetscher et al.[26] Hohenwarter et al.[27] and Leitner et al.[29] it is believed that the crack propagated more along the circumference as crack growth along the microstructure alignment is easier than in the interior where the microstructure is more isotropic. In addition, the torsional load (shear strain amplitude) is higher along the circumference.

In **Figure 17** and **18**, Lagrange strain fields from the DIC measurements are shown for PD0 and PD6, respectively, at the first load cycle and after subsequent cyclic loading when a crack propagated some distance. The Lagrange strain tensor is
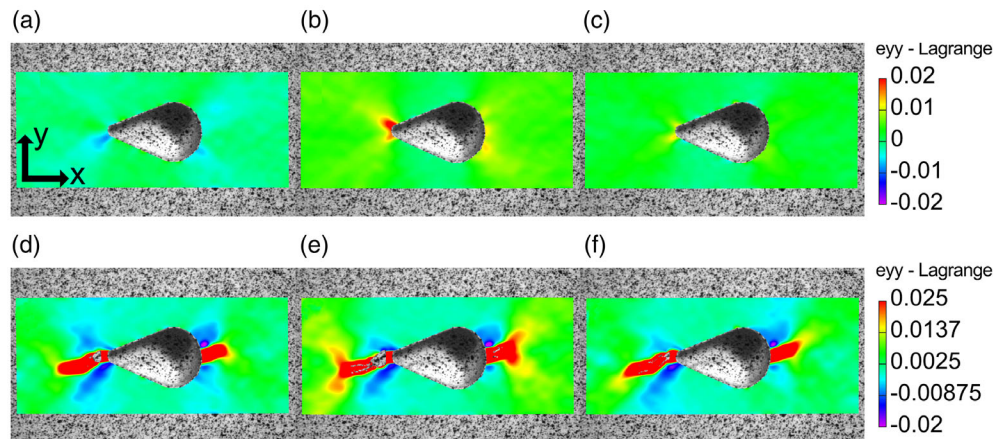
Figure 17. DIC measurement of the PD0 test bar. a–c) the axial strain in the y direction for the first load cycle at the levels: a) $\varepsilon = 0.084\%$ and $\gamma = 0.68\%$; b) $\varepsilon = 0.41\%$ and $\gamma = -0.09\%$; and c) $\varepsilon = 0.08\%$ and $\gamma = -0.72\%$. d–f) the corresponding strain field at cycle 360 at the levels d) $\varepsilon = 0.015\%$ and $\gamma = 0.74\%$; e) $\varepsilon = 0.4\%$ and $\gamma = 0.23\%$; f) $\varepsilon = -0.014\%$ and $\gamma = -0.74\%$.
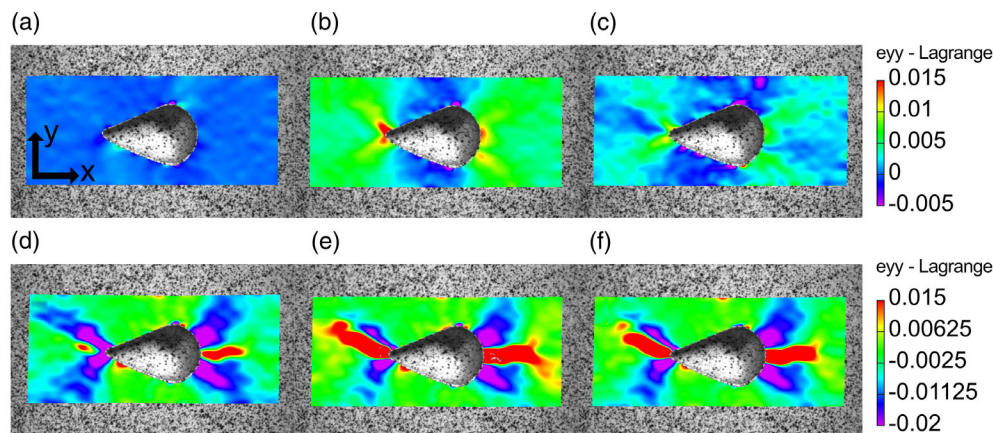
Figure 18. DIC measurement of the PD6 test bar. a–c) the axial strain in the y direction for the first load cycle at the levels: a) $\varepsilon = 0.11\%$ and $\gamma = 0.68\%$, b) $\varepsilon = 0.41\%$ and $\gamma = 0.03\%$, and c) $\varepsilon = 0.13\%$ and $\gamma = -0.67\%$. d–f) the corresponding strain field in cycle 261 at the levels d) $\varepsilon = -0.09\%$ and $\gamma = 0.64\%$, e) $\varepsilon = 0.41\%$ and $\gamma = -0.03\%$, and f) $\varepsilon = 0.09\%$ and $\gamma = -0.66\%$.

2400950 (11 of 13)

derived from the deformation gradient tensor $\mathbf{F}$ and calculated according to Equation (5) where $\mathbf{C}$ is the Cauchy–Green deformation tensor as defined in Equation (6) and $\mathbf{I}$ is the identity tensor. During the first load cycle (a–c), it is observed that the strain field is similar for PD0 and PD6. As the crack initiated and propagated some distance (d–f), the strain intensity colorized in red during tension (e) can be assumed to include the crack tip as crack opening is expected in tension. It is interesting to note that the crack tip on the left side is unaffected at near-pure torque loading for PD6, whereas localized strain can be observed at the crack tip for PD0. This observation shows that the strain at the crack tip is dependent on the orientation of the crack relative the load. Thus, differences in crack path alone are not sufficient to explain crack propagation rate and crack path

$$\mathbf{E} = \frac{1}{2}(\mathbf{C} - \mathbf{I}) \tag{5}$$

$$\mathbf{C} = \mathbf{F}^{\mathrm{T}} \cdot \mathbf{F} \tag{6}$$

4. Conclusion

In this article, we have investigated the effect of large shear deformation on the fatigue characteristics of the pearlitic rail steel R260 subjected to strain-controlled multiaxial fatigue loading. We considered undeformed material and three deformed material states corresponding to the material state at different depths from the highly deformed surface material found in used rail heads. The main findings are the following: 1) The crack path is strongly influenced by the degree of predeformation. Increasing the predeformation causes the surface crack to propagate closer in parallel to the direction of microstructure alignment. For the material state predeformed to a surface shear strain of $\gamma = 1.38$, the crack propagated close to the direction of microstructure alignment, whereas for $\gamma = 0.7$, the crack path is almost horizontal which means the crack propagates at a larger angle to the microstructure alignment; 2) The final crack surface crack length prior final fracture is much shorter for the material state predeformed to a surface shear strain of $\gamma = 0.7$ where the crack path is horizontal as compared to the other material states which show an inclined crack path; 3) The surface crack propagation rate is similar for all material states for the first millimeter of crack growth but because of the variation of surface crack propagation rate for longer cracks it is not possible to determine if there is a difference in crack propagation rate between the material states; and 4) The predeformed material states cyclically soften when subjected to nonproportional multiaxial fatigue loading in agreement to what is observed for uniaxial strain-controlled fatigue loading.
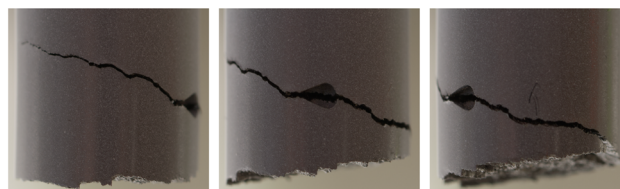
Appendix

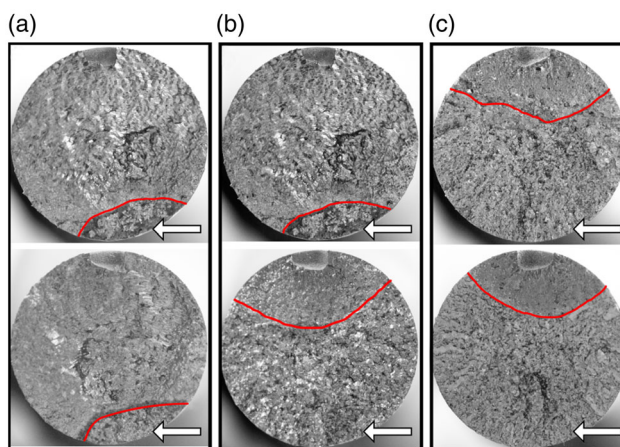### Crack path and fracture surface

A1–A3
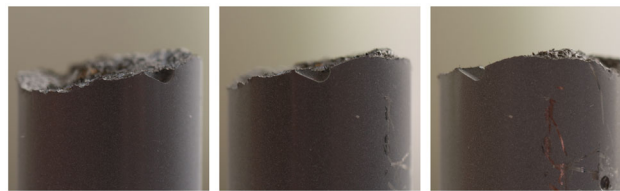
Figure A1. Representative photos of the crack path of a PD0 test bar at different angles relative to the notch.

Figure A2. Representative photos of the crack path of a PD6 test bar at different angles relative to the notch.

Figure A3. Fracture surfaces of the material states: a) PD0, b) PD1, and c) PD3. The red line shows the approximate transition between the fatigue zone and final fracture and the arrow points on the residual fracture zone.

Conflict of Interest

The authors declare no conflict of interest.

Data Availability Statement

The data that support the findings of this study are available from the corresponding author upon reasonable request.

[1] A. Ekberg, *Wear* **1997**, *211*, 280.

[2] A. Bernasconi, M. Filippini, S. Foletti, D. Vaudo, *Int. J. Fatigue* **2006**, *28*, 663.

[3] A. Ekberg, E. Kabo, *Wear* **2005**, *258*, 1288.

[4] F. A. Alwahdi, A. Kapoor, F. J. Franklin, *Wear* **2013**, *302*, 1453.

[5] B. Dylewski, M. Risbet, S. Bouvier, *Proc. Eng.* **2015**, *133*, 202.

[6] C. G. He, H. H. Ding, L. B. Shi, J. Guo, E. Meli, Q. Y. Liu, A. Rindi, Z. R. Zhou, W. J. Wang, *Mater. Charact.* **2020**, *164*, 110333.

[7] G. Schnalzger, W. Daves, R. Pippan, J. Maierhofer, A. Hohenwarter, *Eng. Failure Anal.* **2022**, *140*, 106567.

[8] D. I. Fletcher, F. J. Franklin, A. Kapoor, in *Wheel-Rail Interface Handbook* (Eds: R. Lewis, U. Olofsson), Woodhead Publishing, Cambridge, UK **2009**, pp. 280–310.

[9] U. Zerbst, K. Mädler, H. Hintze, *Eng. Fract. Mech.* **2005**, *72*, 163.

[10] L. Reis, B. Li, M. de Freitas, *Int. J. Fatigue* **2014**, *67*, 191.

[11] C. L. Pun, Q. Kan, P. J. Mutton, G. Kang, W. Yan, *Int. J. Fatigue* **2014**, *66* 138.

[12] G. Kang, Q. Gao, *Mech. Mater.* **2002**, *34*, 809.

[13] X. Xu, L. Ding, H. Miao, Z. Wen, R. Chen, Q. Kan, G. Kang, *Int. J. Fatigue* **2023**, *168*, 107480.

[14] S. Dhar, J. Ahlström, X. Zhang, H. K. Danielsen, D. J. Jensen, *Metall. Mater. Trans. A* **2020**, *51*, 5639.

[15] H. Sunwoo, M. Fine, M. Meshii, D. H. Stone, *Metall. Trans. A* **1982**, *13*, 2035.

[16] J. Ahlström, B. Karlsson, *Wear* **2005**, *258*, 1187.

[17] N. Talebi, J. Ahlström, M. Ekh, K. A. Meyer, *Int. J. Fatigue* **2024**, *182*, 108227.

[18] J. Toribio, B. González, J.-C. Matos, F.-J. Ayaso, *Metals* **2016**, *6*, 12.

[19] M. Jablonska, F. Lewandowski, B. Chmiela, Z. Gronostajski, *Materials* **2023**, *16*, 19.

[20] J. Fei, G. Zhou, J. Zhou, X. Zhou, Z. Li, D. Zuo, R. Wu, *Metals* **2023**, *13*, 2.

[21] X. C. Li, H. H. Ding, W. J. Wang, J. Guo, Q. Y. Liu, Z. R. Zhou, *Tribol. Int.* **2021**, *163*, 107152.

[22] S. Behera, R. K. Barik, S. M. Hasan, R. Mitra, D. Chakrabarti, *Metall. Mater. Trans., A* **2022**, *53*, 3853.

[23] X. L. An, Z. D. Liu, L. T. Zhang, Y. Zou, X. J. Xu, C. L. Chu, W. Wei, W. W. Sun, *Acta Mater.* **2022**, *227*, 117700.

[24] P. Pointner, A. Joerg, J. Jaiswal, Deliverable report D4.1.5GL Integrated Project (IP) Definitive guidelines on the use of different rail grades, INNOTRACK GUIDELINE, Technical report.

[25] S. Maya-Johnson, A. J. Ramirez, A. Toro, *Eng. Fract. Mech.* **2015**, *138*, 63.

[26] F. Wetscher, R. Stock, R. Pippan, *Mater. Sci. Eng., A* **2007**, *445–446*, 237.

[27] A. Hohenwarter, A. Taylor, R. Stock, R. Pippan, *Metall. Mater. Trans. A* **2010**, *42*, 1609.

[28] C. Kammerhofer, A. Hohenwarter, S. Scheriau, H. Brantner, R. Pippan, *Mater. Sci. Eng., A* **2013**, *585*, 190.

[29] T. Leitner, G. Trummer, R. Pippan, A. Hohenwarter, *Mater. Sci. Eng., A* **2018**, *710*, 260.

[30] T. Leitner, A. Hohenwarter, R. Pippan, *Int. J. Fatigue* **2019**, *124*, 528.

[31] K. A. Meyer, D. Nikas, J. Ahlström, *Wear* **2018**, *396–397*, 12.

[32] K. A. Meyer, M. Ekh, J. Ahlström, *Int. J. Solids Struct.* **2018**, *130–131*, 122.

[33] D. Gren, J. Ahlström, *Metals* **2023**, *13*, 10.

[34] D. Nikas, X. Zhang, J. Ahlström, *Mater. Sci. Eng., A* **2018**, *737*, 41.

[35] K. A. Meyer, M. Ekh, J. Ahlström, *Eur. J. Mech., A* **2020**, *82*, 103977.